Compliant DNA Origami Nanoactuators as Size-Selective Nanopores

Yu, Ze; Baptist, Anna V.; Reinhardt, Susanne C.M.; Bertosin, Eva; Dekker, Cees; Jungmann, Ralf; Heuer-Jungemann, Amelie; Caneva, Sabina

Important note
To cite this publication, please use the final published version (if applicable).
Please check the document version above.

Compliant DNA Origami Nanoactuators as Size-Selective Nanopores

Ze Yu, Anna V. Baptist, Susanne C. M. Reinhardt, Eva Bertosin, Cees Dekker,
Ralf Jungmann, Amelie Heuer-Jungemann,* and Sabina Caneva*

Biological nanopores crucially control the import and export of bio molecules across lipid membranes in cells. They have found widespread use in biophysics and biotechnology, where their typically narrow, fixed diameters enable selective transport of ions and small molecules, as well as DNA and peptides for sequencing applications. Yet, due to their small channel sizes, they preclude the passage of large macromolecules, e.g., therapeutics. Here, the unique combined properties of DNA origami nanotechnology, machine-inspired design, and synthetic biology are harnessed, to present a structurally reconfigurable DNA origami MechanoPore (MP) that features a lumen that is tuneable in size through molecular triggers. Controllable switching of MPs between 3 stable states is confirmed by 3D-DNA-PAINT super-resolution imaging and through dye-influx assays, after reconstitution of the large MPs in the membrane of liposomes via an inverted-emulsion cDICE technique. Confocal imaging of transmembrane transport shows size-selective behavior with adjustable thresholds. Importantly, the conformational changes are fully reversible, attesting to the robust mechanical switching that overcomes pressure from the surrounding lipid molecules. These MPs advance nanopore technology, offering functional nanostructures that can be tuned on-demand – thereby impacting fields as diverse as drug delivery, biomolecule sorting, and sensing, as well as bottom-up synthetic biology.

1. Introduction

Transmembrane nanopores are nanoscale channels that span biological membranes and play a vital role in many biological processes, such as cell communication and signal transduction.[1] Built from pore-forming proteins, biological nanopores have been repurposed with great success for biotechnological applications, such as DNA and protein sequencing,[2] sensing of biomarkers and post-translational modifications,[3] monitoring of reaction trajectories, and small molecule delivery.[4] However, their small (typically <5 nm) and fixed diameters restrict their versatility and therefore application range. The size limitations preclude sensing and transmembrane transport of large macromolecules, for example clinically relevant polymers and proteins. Thus, the generation of nanopores with wider, tuneable diameters will expand their application profile and help address challenges in macromolecule delivery, as well as provide a platform for protein (dis-)aggregation studies and synthetic cell research. For example, by mimicking components such as the nuclear pore complex, which in nature consist of large (>40 nm) channel diameters,[5] they would allow better understanding and bottom-up engineering of the selective transport of cargo across the nuclear envelope.

A breakthrough in this direction has been the emergence of synthetic nanopores, which are expanding the field of nanopore technology by providing a pathway to overcome the size

Z. Yu, S. Caneva
Department of Precision and Microsystems Engineering
Delft University of Technology
Mekelweg 2, Delft 2628 CD, The Netherlands
E-mail: s.caneva@tudelft.nl

A. V. Baptist, S. C. M. Reinhardt, R. Jungmann, A. Heuer-Jungemann
Max Planck Institute of Biochemistry
Am Klopferspitz 18, 82152 Martinsried, Bavaria, Germany
E-mail: heuer-jungemann@biochem.mpg.de

A. V. Baptist, S. C. M. Reinhardt, R. Jungmann, A. Heuer-Jungemann
Germany and Center for NanoScience
Ludwig-Maximilians-Universität
Geschwister-Scholl-Platz 1, 80539 Munich, Bavaria, Germany

S. C. M. Reinhardt, R. Jungmann
Faculty of Physics
Ludwig-Maximilians-Universität
Geschwister-Scholl-Platz 1, 80539 Munich, Bavaria, Germany

E. Bertosin, C. Dekker
Department of Bionanoscience
Kavli Institute of Nanoscience
Delft University of Technology
Delft 2629 HZ, The Netherlands

**ADVANCED
SCIENCE NEWS**

www.advancedsciencenews.com

**ADVANCED
MATERIALS**

www.advmat.de

restrictions of naturally occurring protein pores.[1,6] De novo design offers an opportunity to generate nanopores with tailored sizes, shapes, and functionalities far beyond their biological counterparts.[7–12]

In recent years, DNA has become a very attractive building material for the bottom-up design of diverse nanoarchitectures, including nanopores.[8] In particular, the DNA origami technique allows for the precise self-assembly of nanostructures by folding a long single-stranded DNA (ssDNA) scaffold with many short DNA oligonucleotides ("staples"), into designer 2D and 3D shapes.[13–14] The programmability and molecular resolution of this approach enable the formation of transmembrane nanopores with precise geometries and sizes, as well as controllable gating mechanisms. DNA origami-based nanopores with lumens ranging from 5 to 35 nm in diameter have been demonstrated in a number of previous works.[8–9,15–23] Additional functionalities, such as gating via DNA locking/unlocking strands,[24] opening/closing a "lid",[12] or reversibly attaching polymer brushes inside the channel to block biomolecule translocation,[22] have also been reported. However, to date, most reported DNA origami nanopores have been static, meaning that while access to the channel can be controlled, the diameter cannot be modulated on-demand. It remains challenging to realize fully reconfigurable nanopores capable of controlled and reversible conformational changes in both expansion and contraction (opening and closing), and with fully retained functionality after incorporation into operationally relevant environments, e.g. in a lipid membrane. A first step toward this was recently demonstrated in a responsive, semi-flexible DNA origami nanopore that adapted to biochemical (DNA and protein binding) and physical (transmembrane voltage) stimuli. However, this mainly resulted in irreversible opening or closing of the nanopores, somewhat limiting their applicability.[25] Thus, the formation of a fully reconfigurable DNA nanopore with a large lumen size and controlled, reversible initiation and stabilization of different, pre-designed states, able to function in liposomes, yet remains to be realized.

A promising route toward the fabrication of such fully controllable artificial transmembrane channels from DNA origami is the implementation of a compliant mechanism for the pre-programmed opening and closing of the nanopores. Such compliant mechanisms are used to achieve force and motion via the elastic deformation of the components of a flexible device.[26–30] They have been realized experimentally in DNA origami nanoactuators[31] and multi-reconfigurable DNA nanolattices,[32] showing that nanodevices made from DNA can undergo large conformational changes in a precise and controlled manner.

Here, we introduce such a compliant mechanism to design a fully reconfigurable transmembrane DNA origami nanopore, hereafter referred to as the MechanoPore (MP). This MP is capable of controllably switching between 3 configurations (closed ↔ intermediate ↔ open) in response to an external trigger, with resulting nanopore areas ranging from ∼100 nm² to 500 nm². The incorporation of flexible ssDNA linkers and struts in the design allows for the fully reversible switching of the nanopore (via strand addition and displacement) as well as the stabilization of defined open and closed states, resulting in a high level of control. Importantly, the switching mechanism implemented here enables the controlled operation of the nanopores even after their successful insertion into the lipid membranes of giant unilamellar vesicles (GUVs), enabling on-demand translocation of molecules through the pore that is size-selective, i.e., allowing small molecules to pass while blocking transport of large molecules. Our results clearly show that the very same DNA origami nanopores can allow or block the transmembrane passage of macromolecules of certain sizes depending on their adjusted configuration, demonstrating their potential for precisely controlled size-selective molecular transport across lipid membranes. This work paves the way toward the development of DNA-based nanopores for biomedical applications, including targeted drug delivery and molecular sorting, as well as to gateable communication channels in synthetic cell research.

2. Results and Discussion

2.1. Design and Assembly of a Compliant DNA Origami Nanoactuator

Our mechanically actuatable MP consists of a rhombic structure composed of 4 flipped "L"-shaped subunits made up of 22 helix bundles designed in a honeycomb lattice in order to minimize global twist (see Figures S1 and S2 Supporting Information for caDNAno[33] layout). In a subunit, the bottom part forms the transmembrane section that embeds into the lipid bilayer (barrel), and the upper part rests on the top of the membrane (cap). Switchable conformations are realized by the incorporation of flexible ssDNA segments made from scaffold parts connecting the adjacent rigid subunits, resulting in some flexibility in the corner regions but limiting out-of-plane movement (**Figure 1a–c**). This design feature allows for full control over the nanopore's configuration via the addition of trigger strands, enabling an active opening and closing mechanism, where the final states are fully stabilized (Figure 1d). In the absence of a trigger strand, the MP is in an "intermediate" state with an opening angle of around 50° and a diameter of the enclosed lumen of around 20 nm. The addition of trigger strands ("opening strands", 24 staples each with a total length of 35 nucleotides (nt), see also Table S1, Supporting information) complementary to the ssDNA regions inside the MP (12 scaffold segments in total, each with a length of 56 nt) results in the formation of double-stranded struts with increased stiffness, causing a conformational change into the open, square-shaped state with an opening angle of around 90° and a significantly increased inner lumen (diameter of ≈30 nm) (see Figure S3a, Supporting information). This active opening mechanism was introduced into the MP to ensure a reliable opening of the structure also, e.g., in the environment of a lipid membrane, where lateral membrane pressure could counteract a stable "fully open" conformation (see also Section S1, Supporting information). In order to controllably switch from the open to the intermediate state, all opening strands were designed with an additional 7-nt toehold region. This allows strand displacement of the opening strands upon the addition of fully complementary invader strands ("anti-opening strands"), making the conformational switching of our MP fully reversible.

Similarly, an active closing mechanism was implemented (Figure S3c, Supporting information). To achieve this, the MP
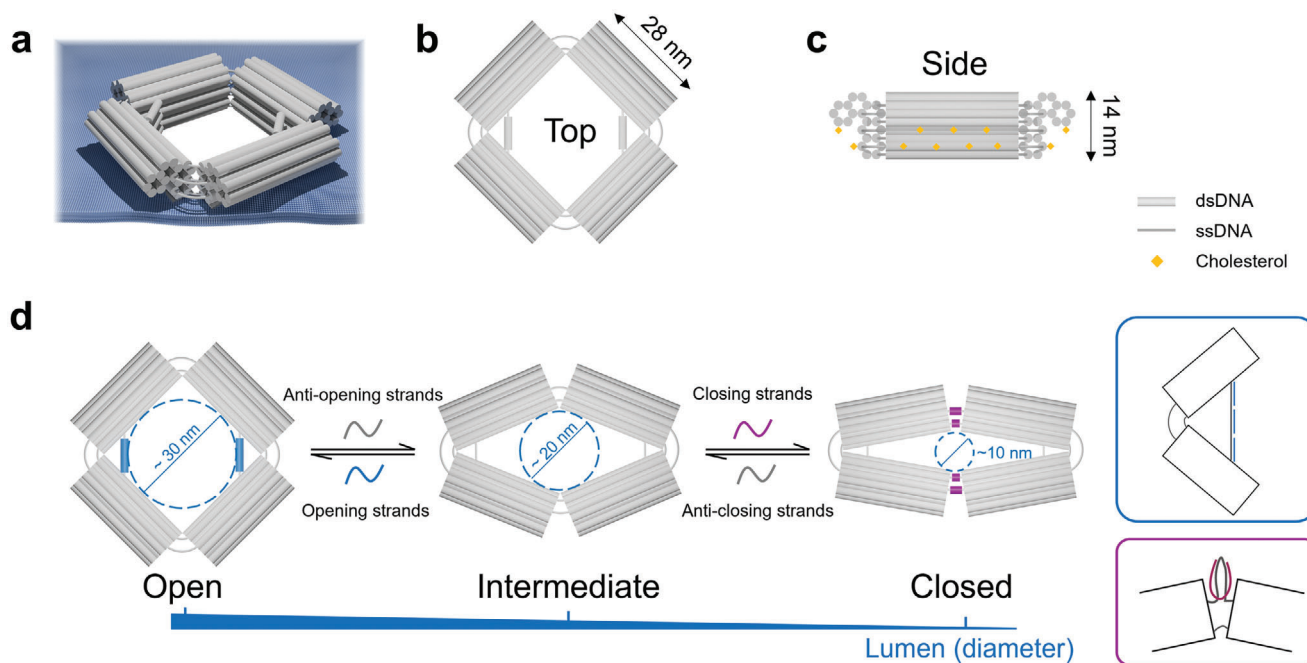
Figure 1. Design and working principle of the reconfigurable MechanoPore. a) 3D illustration of the DNA nanopore in the open state (MP-O) when embedded in a lipid membrane. b) Top and c) side view of MP-O. Grey cylinders represent dsDNA, while the grey lines are ssDNA. Yellow diamonds represent schematically the attached cholesterol modifications. d) Reversible conformational changes between 3 states (open, intermediate, and closed) of the MP in response to the addition of trigger strands (blue and magenta for opening and closing strands, respectively) and anti-trigger strands (grey). Inset: trigger mechanism: the fully open state (blue) and the closed state (magenta).

was designed with flexible orthogonal ssDNA regions in 2 opposing corners (10 scaffold segments per corner, with lengths of 6 nt, 16, 26, and 33 nt, respectively, depending on the distance of the connected helices from the inner lumen). The addition of "closing strands" (14 staples, with total lengths of 21, 28, and 36 nt, respectively) forces the MP into its closed state with a small opening angle of about 20–25° and a significantly reduced inner lumen (diameter of ≈11 nm). Analogously to the active opening mechanisms, this conformational change into the closed state is fully reversible via the addition of the corresponding invader strands ("anticlosing strands") to displace the toehold-containing closing strands. Notably, the anticlosing strands and the opening strands can be added in one step to promote the immediate switching of the MP from its closed into its open state (and vice versa).

To enable the insertion of the MP into the hydrophobic interior of the lipid bilayer, 30 handles for cholesterol-modified DNA strands were introduced, which protrude from the outer surface of the 4 bottom parts of the structure as well as from underneath the 4 caps. The handles are positioned on 2 different helices of the bottom part and the cap, respectively, and they are distributed alongside the 4 subunits with horizontal distances between 6 and 8.5 nm (distances vary due to the design of the core staples). The cholesterol modifications are located in close proximity to the DNA origami (proximal configuration with a 4 nt spacer between the DNA origami and the actual handle sequence, see also Figure S4 and Section S2, Supporting information) in order to keep the aggregation of the DNA origami structures to a minimum.[34] The MP also features up to six handles for the attachment of Cy5-modified DNA strands for fluores-

cence imaging (see Figure S1 for details of the positioning of the handles).

2.2. Structural Characterization

After the assembly of the MP, we initially assessed the quality of the folded structures by agarose gel electrophoresis (AGE) and negative-stain transmission electron microscopy (TEM), (**Figure 2**; Figure S5, Supporting information). As can be seen from the respective images in Figure 2a–c, well-formed nanopores were obtained for the 3 different states. Their global shapes match well with the design of the 3 conformations, in which 4 rigid edges enclose the rhombus-shaped pore structure. The dsDNA struts stabilizing the open state can clearly be seen in the TEM micrographs as well as in the 2D classification images. The measured opening angles of the three states were determined to be approximately 85 ± 11° (open; error represents standard deviation S.D.), 46 ± 8° (intermediate), and 24 ± 8° (closed), respectively, as obtained from the TEM micrographs (a comparison between the measured and theoretical features of the MP in its different states can be found in Table S2, Supporting information). The respective lumen sizes were determined to be 496 ± 160 nm^2 (open), 350 ± 106 nm^2 (intermediate), and 194 ± 144 nm^2 (closed) (see Figure 2d). In principle, a variety of fixed opening angles of the MP can be achieved by tuning the lengths of the double-stranded regions and the single-stranded loops in the struts by choosing a different set of opening staples (see Figures S3b and S6, Supporting information).
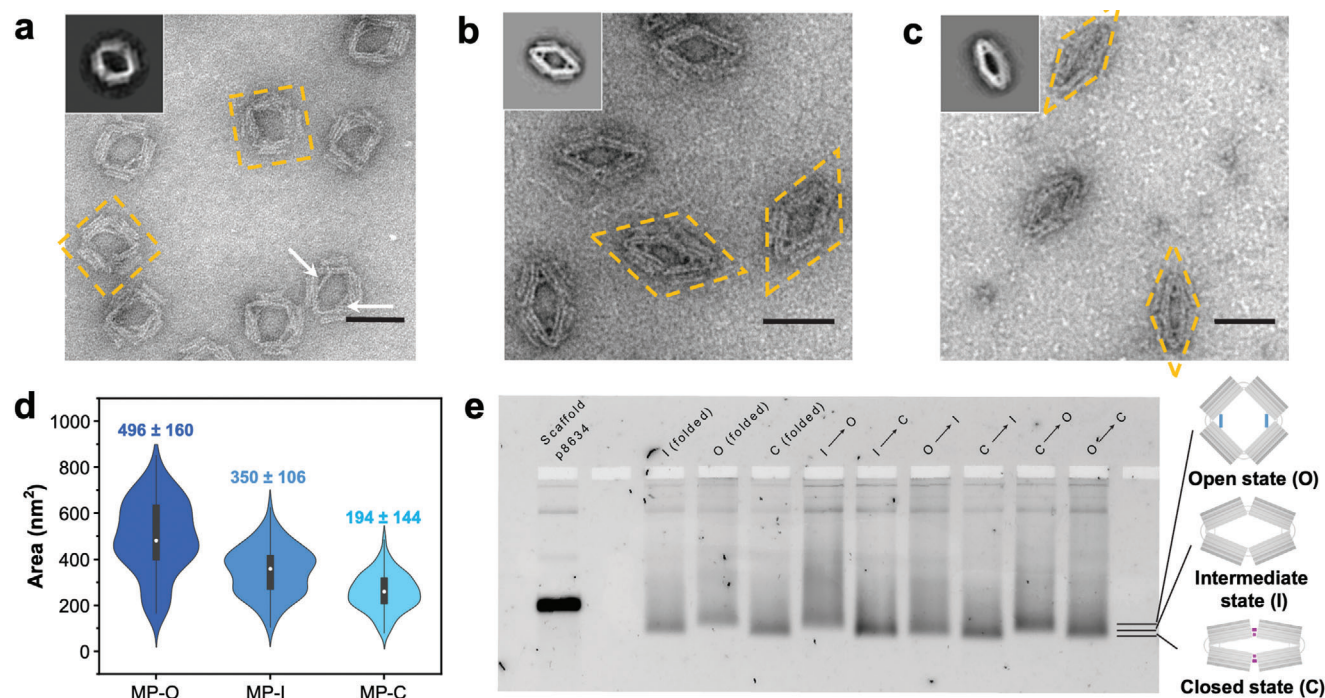
ADVANCED
SCIENCE NEWS
www.advancedsciencenews.com

ADVANCED
MATERIALS
www.advmat.de

Figure 2. Negative-stain TEM images, 2D classification, and AGE of the MP in its different configurations. a–c) TEM images of the MP in its open, intermediate, and closed states. Insets: class averaging for 90 particles. Yellow dashed lines outline the shapes of representative structures in the TEM images. White arrows point to the double-stranded struts of the MP in the open state. Scale bars: 50 nm. d) Statistical analyses of the inner area of the MPs in the open (N = 145), intermediate (N = 179), and closed (N = 164) states. Error: S.D. e) Agarose gel of the MPs that were folded in different configurations or switched between different states in solution.

From the gel image in Figure 2e it can also be seen that the 3 states display slight differences in their electrophoretic mobility. Structures in the open state exhibit the slowest electrophoretic mobility, while structures in the closed state display the highest mobility. This can be easily explained by the effective overall volume increase from the closed to the open state. Although the intermediate state is an equilibrium between the open and the closed state, as it is not stabilized by external triggers, both the TEM analysis and AGE show that intermediate structures adopt a preferred conformation with an average opening angle of 50° and display an intermediate electrophoretic mobility between the open and the closed state.

In order to investigate the switching behavior of the MPs, we performed 3D-DNA-PAINT[35] super-resolution microscopy as well as monitoring the electrophoretic mobility after the addition of the respective trigger strands. As can be seen in Figure 2e, shifts in electrophoretic mobility according to the structural change induced by the trigger strands can be observed as desired. We also investigated the timescale on which the switching between different states can be performed. For nanopore switching in solution, incubation at elevated temperatures (here 37 °C) accelerated the switching and reduced the time needed for successful conformational changes in all directions (I → O, I → C, C → O, and O → C) down to several minutes (see Figure S7, Supporting information). At room temperature, full switching into the different states was achieved after an incubation of around 30 min. DNA-PAINT is an implementation of Single-Molecule Localization Microscopy (SMLM) which achieves nanometer resolution by precisely localizing individual fluorophores in a set

of diffraction-limited images. Specifically, DNA-PAINT relies on the transient binding of a diffusing dye-coupled DNA imager strand to a sequence-complementary docking site on the sample. Upon binding of an imager strand to a target, a fluorophore is detected as a signal spot on the camera. Over the duration of an imaging round, the available signals from the targets in the region of interest are recorded and a super-resolution image is then reconstructed.[35] To analyze the switching behavior in situ with 3D-DNA-PAINT, the MPs were anchored to a glass surface via neutravidin-biotin interactions (biotin handles located at the bottom part of only one of the 4 subunits; Figure S2, Supporting information). DNA-PAINT docking sites were positioned at the 2 opposing corners of the MPs without the struts, allowing for distance monitoring between the corners (see **Figure 3**; Figure S2, Supporting information). In the case of closed MPs, the distance between the binding sites might be smaller than the resolution of DNA-PAINT,[37] thus leading to overlapping signals from the 2 corners of the MPs which could result in the erroneous exclusion of MPs with narrow opening angles from the data analysis. For reliable and unbiased distance measurements independent of the MP state, we employed a variant of DNA-PAINT called Resolution Enhancement by Sequential Imaging[36] (RESI). Labeling opposing corners with orthogonal imager binding sites and sequentially imaging them allows us to unambiguously distinguish between the signals from the 2 corners.[37] Thus, the coordinates of the corners can be reliably identified and the distance between them can be precisely determined (see Methods and Figure S9, Supporting information for details about the image analysis).

**ADVANCED
SCIENCE NEWS**

www.advancedsciencenews.com

**ADVANCED
MATERIALS**

www.advmat.de
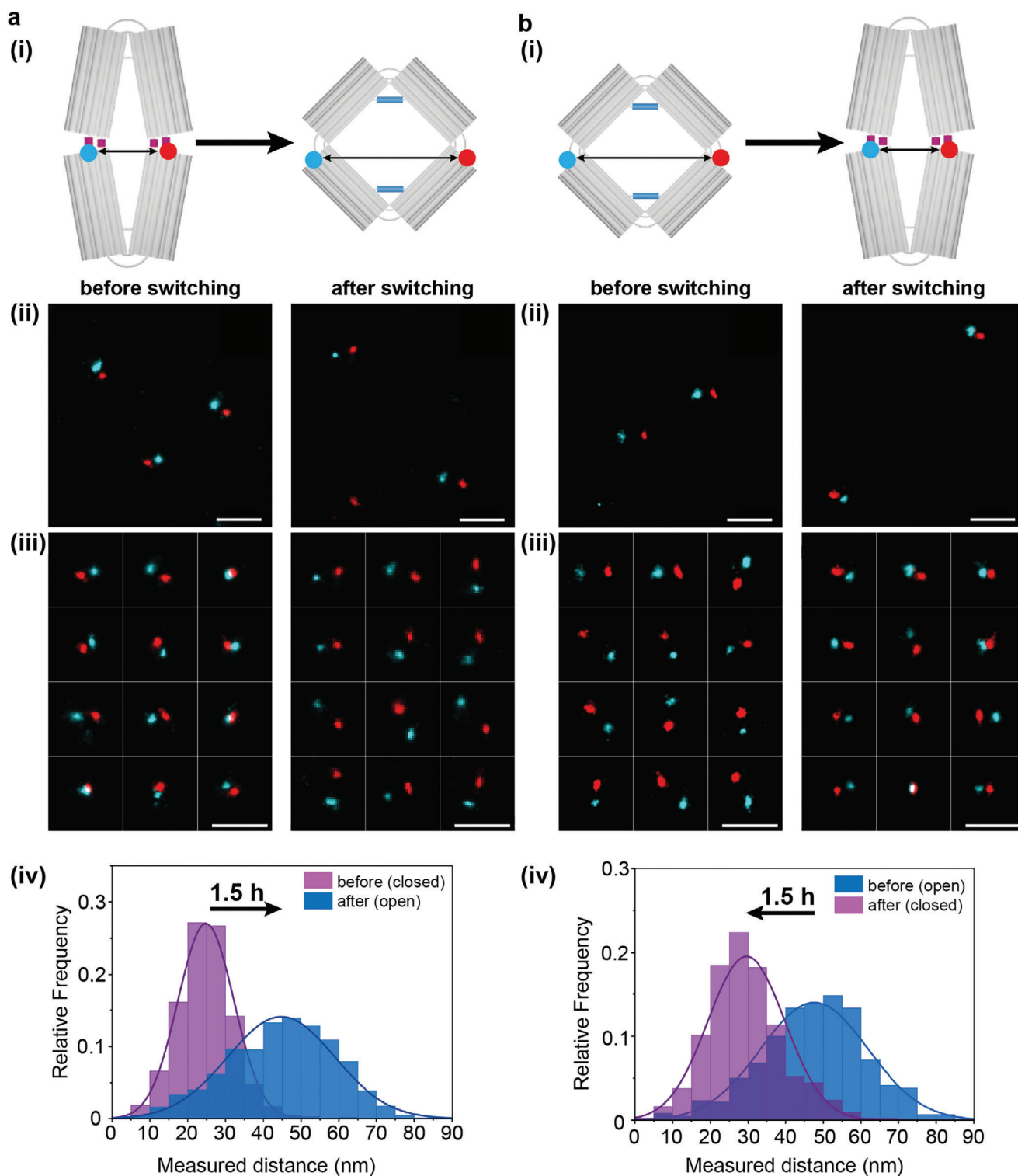
Figure 3. 3D-DNA-PAINT measurements on MPs. a) Conformational change from closed to open state with an incubation time of 90 min. b) Conformational change from open to closed state after 90 min of incubation with the respective trigger and anti-trigger strands. Schematic representation of the switching of the MPs for the respective experiment i), representative fields of view from all datasets ii), an overview over representative nanopores selected during data analysis, clearly showing the shift in the observed distances iii) and the respective distance distributions (N > 700) for the switching experiments iv). Scale bars: 100 nm.

**ADVANCED
SCIENCE NEWS**

www.advancedsciencenews.com

**ADVANCED
MATERIALS**

www.advmat.de

We initially performed measurements on MPs pre-formed in the open, intermediate, and closed states (see Figure S8, Supporting information). The distance distributions obtained from the different nanopore configurations exhibit mean distances of 26.0 ± 8.4 nm ($\mu \pm \sigma$ of a fitted normal distribution, closed state), 36.2 ± 12.1 nm (intermediate state) and 47.5 ± 16.4 nm (open state) which match the expectations from the design and the characterization via TEM, taking into account the positions of the imager binding sites on the nanopore caps (Figure 2 and Figure S5, Supporting information). As a next step, we demonstrated in situ switching. We first performed a complete 3D-DNA-PAINT measurement on the MPs in their closed state. Then, the slide was thoroughly washed to remove all imager strands. After that, both the anti-closing strands and the opening strands were added in a twentyfold molar excess to the channel, and the slide was incubated at 33 °C (a slightly elevated temperature was chosen to promote accelerated switching). In order to probe the time scale of the switching, we investigated 2 different incubation times (90 min and 3 h). After this, excess trigger strands were flushed out of the channel and a second full 3D-DNA-PAINT measurement was performed. Figure 3a shows the distance distributions for the MPs before and after the incubation with the trigger strands for 90 min, representative sections (fields of view, FOVs) from the aligned datasets, and an overview of representative selected nanopores. The sample in the closed state exhibits a distance distribution with a peak centered at around 24.8 ± 7.4 nm which corresponds to an opening angle of around 20–24°, taking into account the positions of the handles on the MPs. After the switching procedure, the main peak in the distance distribution is shifted to 44.7 ± 14.2 nm, showing a successful conformational change to the open state. A similar behavior could be observed after the longer incubation time of 3 h (Figure S9, Supporting information), suggesting that 90 min is already sufficient. In both experiments, the obtained distance distributions closely correlate to those obtained for MPs pre-folded into the open state. To demonstrate full reversibility, we next tested the reverse switching of the MPs from the open into the closed state. Figure 3b shows representative FOVs from the data sets, examples for selected MPs, and the corresponding distance distributions for the sample before and after incubation with the anti-opening and the closing strands at 33 °C for 90 min. Again, we observed a pronounced shift of the mean of the distance distribution from around 47.6 ± 14.3 nm in the initial state to around 28.6 ± 10.2 nm, clearly demonstrating the successful switching to the closed state. Additionally, we aimed to test the robustness of the switching mechanisms and carried out repeated switching (in total six times) of the same MP sample between the closed and the open state by incubating the sample with the respective trigger and anti-trigger strands at 33 °C for 30 min in each round, followed by DNA-PAINT imaging. The obtained distance distributions confirmed the successful conformational changes of the MPs for each switching round. Figure S10 (Supporting information) shows a clear shift in the mean of the distributions after each switching procedure. Even after six rounds of switching, the nanopore sample did not show significant signs of degradation. After the fourth switching (from open to closed), a small fraction of nanopores remained in the open state; this can possibly be attributed to an incomplete displacement of the opening strands and the dominance of the open state over the closed state

if both types of trigger strands are present in the sample (see also Figure S11, Supporting information). These results confirm the robustness of the nanomechanical switching capabilities of the MPs.

2.3. Reconstitution and Permeability of MPs in Lipid Bilayers

After successful characterization of the MPs and confirmation of their controlled conformational switching in situ, we next tested their ability to insert into a lipid membrane. The insertion of large DNA origami nanopores into lipid membranes is far from trivial. As DNA molecules are hydrophilic, DNA nanostructures cannot penetrate the membrane spontaneously without lipidation by, e.g., cholesterol modification. The number of cholesterol modifications required for successful insertion strongly depends on the size of the structure, and the incorporation of many cholesterol-modified staples can cause aggregation of the nanostructures.[34] However, the correct positioning of cholesterol modifications on the DNA origami (distance between adjacent modifications, handle lengths, etc.) can reduce the risk of aggregation. As can be seen in Figure S4, we do not observe significant aggregation or clustering of the nanostructures after cholesterol addition.

A further challenge is that large DNA nanostructures can adopt various orientations when inserted into the membrane and the incorporation yield of functional membrane-spanning pores can be very low. While the embedding of small DNA origami nanopores into lipid membranes can often rely on spontaneous insertion into preformed lipid bilayers, the probability of insertion of large nanopores decreases dramatically with increasing size of the pores.[22] To address these challenges, we used the continuous Droplet Interface Crossing Encapsulation (cDICE) method to embed the nanoactuators into GUVs during liposome formation.[11,38] This technique enables efficient incorporation of DNA nanostructures into lipid membranes, resulting in functional GUVs with embedded MPs. The principle of cDICE involves the sequential deposition of buffer solutions (outer layer) and lipid-in-oil suspensions (inner layer) in a rotating chamber (**Figure 4a**). An aqueous solution containing the DNA origami structures (with 2 MDa dextran) is injected into this rotating lipid-in-oil phase. Due to the shear forces generated by the rotation, droplets form and travel through the oil phase, acquiring a lipid monolayer in the process. During the formation of the monolayer, the DNA origami nanopores with cholesterol modifications can be inserted into the lipid. Then, these droplets containing the DNA origami nanopores cross the oil-water interface, pick up a second lipid monolayer, and are ultimately collected in the aqueous phase as GUVs. From a single cDICE round, hundreds of GUVs with a diameter of 11 ± 5 μm (N = 446) can be collected (Figure S12, Supporting information). The use of 2 MDa dextran in the DNA origami solution helps to drive the MPs to the lipid surface and increases their effective density, drastically enhancing their incorporation efficiency.[11] Due to its large size, the 2 MDa dextran remains in the GUV in the presence of MP (even in their open state).

Initially, we used AFM to investigate the occurrence of insertion upon splashing GUVs onto a mica substrate, leading to a flat membrane (Figure S13, Supporting information). After the MP insertion into the GUVs, we found some brighter spots on
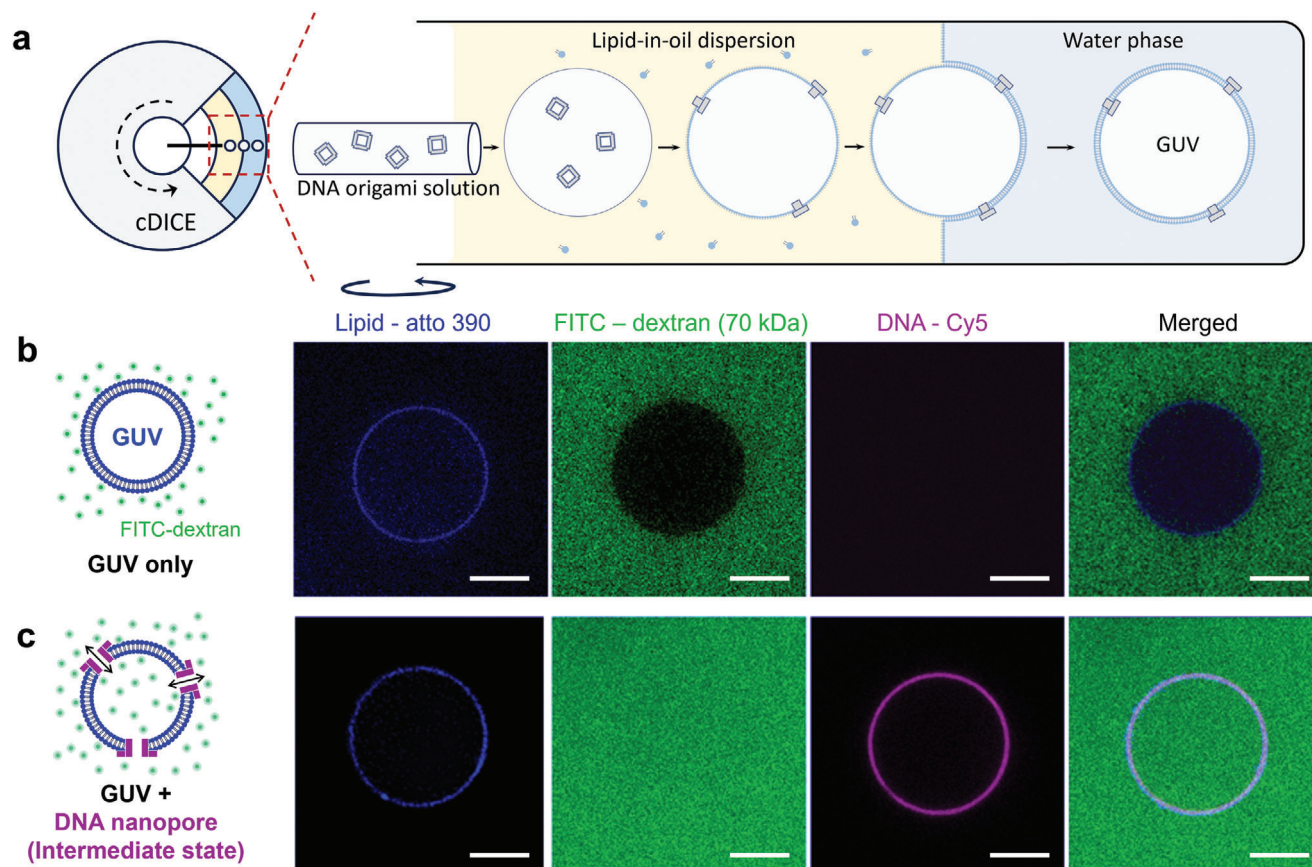
**ADVANCED
SCIENCE NEWS**

www.advancedsciencenews.com

**ADVANCED
MATERIALS**

www.advmat.de

Figure 4. cDICE and permeability of the MPs reconstituted in GUVs. a) Schematic representation of cDICE. The orientation of the MP insertion is determined by the distribution of hydrophilicity of the DNA structure and cholesterol modifications, likely resulting in mixed inward and outward-facing orientations (see also Section S3, Supporting information). b) and (c) are the confocal images of GUV and GUV with the MPs (in the intermediate state), respectively. From left to right, pseudo-colours are blue = atto 390 (GUV), green = FITC (FITC-dextran), magenta = Cy5 (DNA), and the merged channel. Scale bars: 5 µm.

the membrane, which we attribute to the nanopores. A comparison of the heights of the bare lipid membrane, free MPs, and the MPs located on the membrane (≈6, 12, and 5 nm respectively, whereby the last value is measured with respect to the height of the lipid membrane) strongly indicates that a part of the DNA origami structure is embedded into the membrane.

Since the MPs should function as size-selective transmembrane channels, we also investigated their reconstitution and pore-forming capabilities in GUVs using confocal microscopy. We introduced different fluorescence modifications into the lipid membrane of the GUVs (Atto 390, blue channel) and onto the MPs (Cy5, red channel) to visualize their presence and spatial distribution. FITC-modified dextran (molecular weight: 70 kDa, green channel) was used as cargo to test the permeability of the MPs.

In Figure 4, we initially analyzed pure GUVs without any MPs. Confocal imaging clearly shows circular vesicles in the blue channel, while the fluorescence in the red channel is negligible, indicating the absence of MPs. By analyzing the fluorescence intensity in the green channel, we found that most of the GUVs exhibit a large intensity difference between inside and outside of the vesicles, suggesting that the FITC-dextran is unable to enter the GUVs. Quantitatively, we calculated the normalized fluorescence intensity difference $I_{ndiff} = (I_{out} - I_{in}) / I_{out}$ of pure GUVs, which yields 0.21 ± 0.04 (error: S.D., N = 69) consistent with the results of unfilled GUVs from a previous study,[11] where I_{out} and I_{in} are the fluorescence intensities outside and inside the vesicles, respectively (Figure S14, Supporting information). This confirms that the lipid membrane blocks the translocation of the FITC-dextran and is therefore impermeable to such macromolecules. In the next step, MPs in their intermediate state were included in the GUV production with the cDICE technique. In contrast to the negative control, the images show the colocalization of Cy5 fluorescence with the fluorescence signal from the labeled lipids, clearly indicating the presence of MPs that are evenly distributed on the vesicle membrane. It should be noted, however, that the presence of a fluorescence signal does not necessarily imply complete insertion of structures into the lipid membranes. Heterogeneity in GUV samples[39] and the possibility that some DNA nanopores may only adhere to the membrane, not forming full transmembrane channels, resulted in a certain fraction of unfilled GUVs. We therefore analyzed the fluorescence intensity from the FITC-dextran, in order to determine if transmembrane channels were formed. The fluorescence intensity was found to be very similar inside and outside the GUVs ($I_{ndiff} \approx 0$, Figure S14, Supporting information). This suggests that the MPs can be

**ADVANCED
SCIENCE NEWS**

www.advancedsciencenews.com

**ADVANCED
MATERIALS**

www.advmat.de

successfully inserted into lipid bilayers, form transmembrane channels, and enable the transmembrane passage of macromolecules.

Subsequent FRAP assays were used to estimate the diffusion rate of dextran across the nanopores and the average distribution density of the nanopores on the GUV membrane (Figure S15, Supporting information). We compared the fluorescence recovery of pure GUVs and GUVs containing MPs, which were photobleached only in their interior after overnight incubation with 70 kDa FITC-dextran. As expected, an MP-containing GUV showed almost full recovery of fluorescence signal after a few minutes, while a GUV without MPs showed negligible recovery even with a longer time measurement (Figure S15b–e, Supporting information). We then selected the MP-containing GUVs that showed almost equal intensity inside and outside ($I_{ndiff} \approx 0$) and employed the same FRAP assay to fit a diffusion model derived from Fick's first law and estimated the number of nanopores (N_p) in a GUV (Figure S15f, Supporting information). By analyzing the FRAP curves obtained from GUVs with different sizes, we found that the estimated number of pores N_p per GUV varies from a few to several hundred.[11] For a 12 μm diameter vesicle, we estimated the number of functional pores to be $N_p = 125$. While there is a large variation in N_p, we do observe an overall increase in N_p with increasing GUV size, roughly proportional to a cubic fit to the GUV diameter (Figure S15g, Supporting information), which is consistent with the assumption that MPs move from the inner GUV volume to the membrane during GUV formation.

2.4. Size Selectivity of the MechanoPores

Following the successful integration of MPs in GUVs, we set out to test the size-selective transport of macromolecules through MPs with different initial conformations. Here, 10, 70, and 150 kDa FITC-dextrans were used as molecular standards. The gyration diameter of dextrans with different MW can be estimated by the empirical equation $D_g = 0.072 \times MW^{0.48}$,[40] resulting in values of approximately 6, 15, and 22 nm, respectively. Therefore, the transmembrane passage of large 150 kDa FITC-dextran should only be possible if successfully inserted MPs are present in their fully open state, whereas 10 kDa FITC-dextran should be able to pass through the nanopores even in their closed state. Extraction of the FITC fluorescence intensity inside and outside the boundary of GUVs allowed us to calculate the normalized intensity difference I_{ndiff}. By comparing the different behaviors of pure GUVs and GUVs containing MPs, the histograms clearly indicate the existence of 2 types, corresponding to filled GUVs (I_{ndiff}: −0.10–0.09) and unfilled GUVs (I_{ndiff}: 0.09–0.33), (Figure S14, Supporting information). Thus, when I_{ndiff} was lower than 0.09, the corresponding vesicle was marked as filled (see Figure S16, Supporting information, for histograms of I_{ndiff} for 3 independent checks of each state).

The experimental data displayed in **Figure 5** shows the successful incorporation of all 3 different MPs into the GUV as indicated by their fluorescent signal in the membrane. In the open state, 10 kDa dextran (80% ± 9% filled), 70 kDa dextran (64% ± 8% filled), and 150 kDa dextran (46% ± 8% filled) could pass through the nanopores, as expected. MPs in the interme-

diate state only allowed the translocation of the 10 kDa dextran (86% ± 10% filled) and the 70 kDa dextran (55% ± 9% filled), while most of 150 kDa dextran (20% ± 9% filled) was blocked out. In the closed conformation, transmembrane passage ccould only be observed for the 10 kDa dextran (64% ± 7% filled). This indicates that, as designed, from closed to open conformations, the MPs show gradually increasing lumen sizes after insertion into the lipid membrane. This in turn translates into their ability to size-selectively translocate cargo across the lipid membranes or hinder molecules from entering the GUVs.

To further analyze the lumen sizes after incorporation into the lipid membrane, we used TEM analysis of splashed GUVs (Figure S17, Supporting information). Interestingly, the MPs exhibited a decreased average lumen size after membrane insertion (compared to values obtained in the absence of a lipid membrane) for all 3 configurations (O: from 496 ± 160 to 353 ± 110 nm^2; I: from 350 ± 107 to 198 ± 73 nm^2; C: from 194 ± 144 to 118 ± 52 nm^2). This can be attributed to lateral pressure exerted by the lipid membrane, which has been reported to lead to deformations of DNA origami nanopores, reducing the actual lumen size of the nanostructures.[25] Interestingly, however, the intermediate state truly remained as such and did not get compressed to a lumen size close to the closed state. Although we cannot exclude partial deformation of the intermediate state, we can clearly distinguish between the closed and the intermediate state, suggesting that despite the semi-flexible nature of the structure itself, lateral membrane pressure is not strong enough to fully close the structure, and thus confirming the necessity for a controlled closing mechanism.

2.5. In Situ Reversible Conformational Changes of DNA Nanoactuators in Lipid Bilayers

For future applications, it is of great importance that the MP can not only be switched between its different conformations in solution or when anchored to a surface but also when embedded within a lipid membrane, having to exert forces against the lateral membrane pressure. In order to determine the ability of the MPs to reversibly change their conformation also after membrane insertion, we incorporated the MPs in their intermediate state into GUVs and subsequently added the respective trigger (and antitrigger) strands followed by confocal imaging. Dye influx experiments were performed using the 70 kDa FITC-dextran as the standard cargo, as the translocation behavior of this dextran allows for a clear identification of the nanopore conformation.

For this, a sample was divided into five batches that were triggered to undergo a different sequence of conformational changes: 1) intermediate → open, 2) intermediate → open → intermediate with a 2 h interval between each switch, 3) intermediate → closed, 4) intermediate → closed → intermediate with a 2 h interval between each switch, 5) adding buffer as a blank. For each sequence (1-5), we analyzed part of the resulting sample by TEM after 2 h incubation at room temperature, while the remaining part was used for confocal imaging of dye influx with the 70 kDa FITC-dextran after 24 h. Importantly, both TEM analysis (Figure S18, Supporting information) as well as dye influx assays show that conformational switching to an open or closed
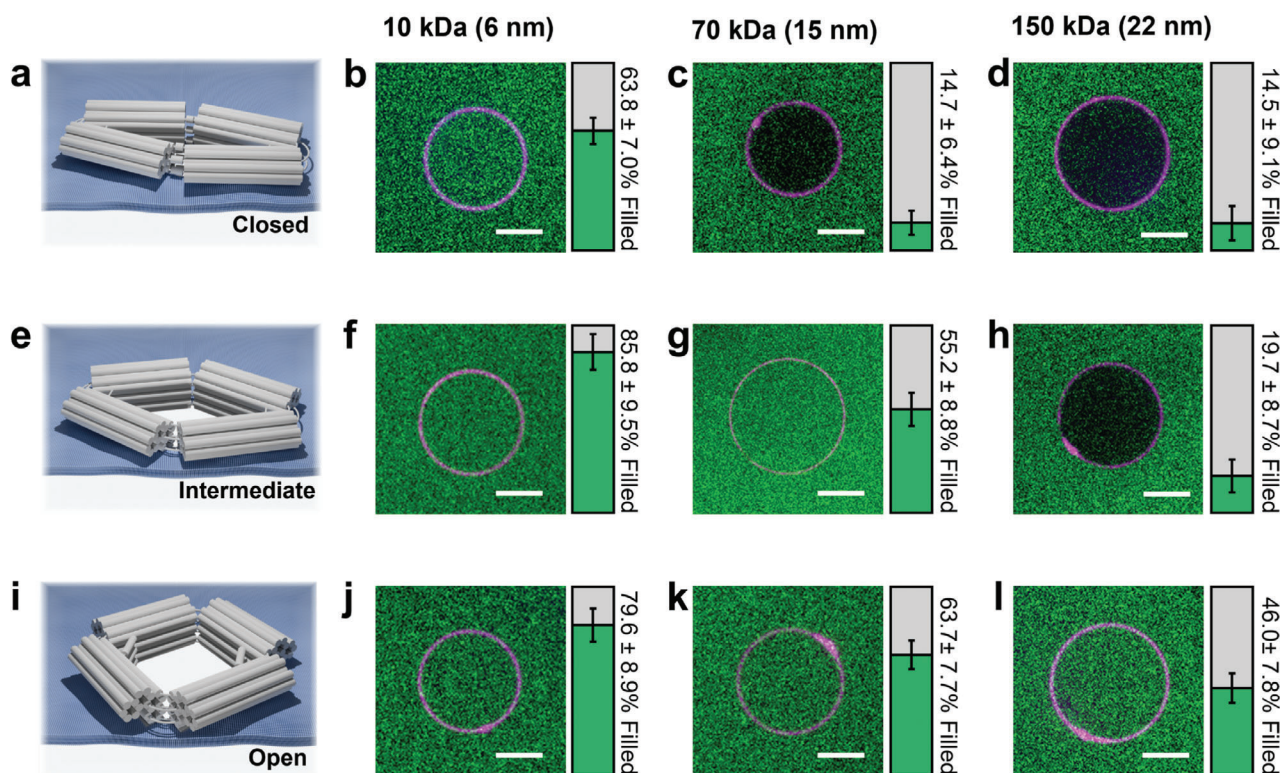
**ADVANCED
SCIENCE NEWS**

www.advancedsciencenews.com

**ADVANCED
MATERIALS**

www.advmat.de

Figure 5. Size-selectivity of 3 different states of MPs. Confocal images of 10, 70, and 150 kDa FITC-dextran influx in closed state a–d), intermediate state e–h), and open state i–l) MPs. Each image shows the representative behavior of more than 150 GUVs. Bar graphs on the right are the percentages of GUVs in which dextran influx is observed. Scale bars: 5 µm. Error bars: S.D.; N > 150 for 3 different experiments.

state as well as reversible switching back to the intermediate state is still possible even after embedding into the lipid membrane.

As can be seen from **Figure 6** (bar percentages are calculated from Figure S19, Supporting information), initially, MPs in the intermediate state showed an almost equal distribution of filled and unfilled GUVs (52% ± 7% filled). After adding the respective trigger strands, the percentage of filled GUVs changed to $66 \pm 8\%$ (intermediate → open) and $27\% \pm 7\%$ (intermediate → closed), respectively. Structures switched from intermediate to open (or closed) and back to the intermediate state (i.e., processes 2 and 4) displayed a similar distribution and percentage of filled GUVs (56 ± 7% and 53 ± 9% filled) as the non-actuated MPs, indicating the achievement of reversibly controllable conformational changes. Interestingly, the incorporation of preformed closed MPs showed a slightly lower percentage of filled GUVs (cf. Figure 5c). We attribute this to a partially sterically hindered position of the closing mechanism after insertion into the lipid membrane. Since the linking regions of the corners (and thereby the regions that are responsible for the active closing mechanism) are located on the outside of the MP, the diffusion of the closing strands to their respective binding sites may be partially obstructed. Nevertheless, after the addition of anti-opening strands, a clear difference between the closed and the intermediate state can be observed. The conformational switching was also confirmed at a single vesicle level during 2 switching cycles and using 2 dextran sizes (70 and 150 kDa). Details of these experiments are shown in Figure S20 and Section S4 (Supporting information).

Overall, these experiments successfully show that active conformational switching and reversible control over the lumen size of DNA origami nanopores can be achieved with at least 3 distinct and stable states.

3. Conclusion

Here, we present a dynamic, three-state reconfigurable DNA origami MechanoPore that exhibits size-selective transport of biomolecules across lipid membranes on-demand. We overcome the challenge associated with reconstitution of the large nanopores (edge length of around 28 nm and ≈500 nm² lumen) in lipid bilayers by using the cDICE technique for direct integration of the MPs in GUVs.

The MPs are designed as nanoactuators that can be robustly switched between 3 distinct conformations in a well-controlled and fully reversible manner via an external trigger mechanism (addition and displacement of DNA strands). The resulting lumen dimensions can thus be tuned from ≈100 to 500 nm². The rationally engineered opening and closing mechanisms actively promote the conformational switching of the MP not only in solution, but also when anchored to a surface and, most importantly, after insertion into lipid membranes.

To the best of our knowledge, this is the first experimental demonstration of reversible switching of a DNA origami transmembrane channel in lipid membranes with multiple well-defined structural states. We confirm the nanomechanical
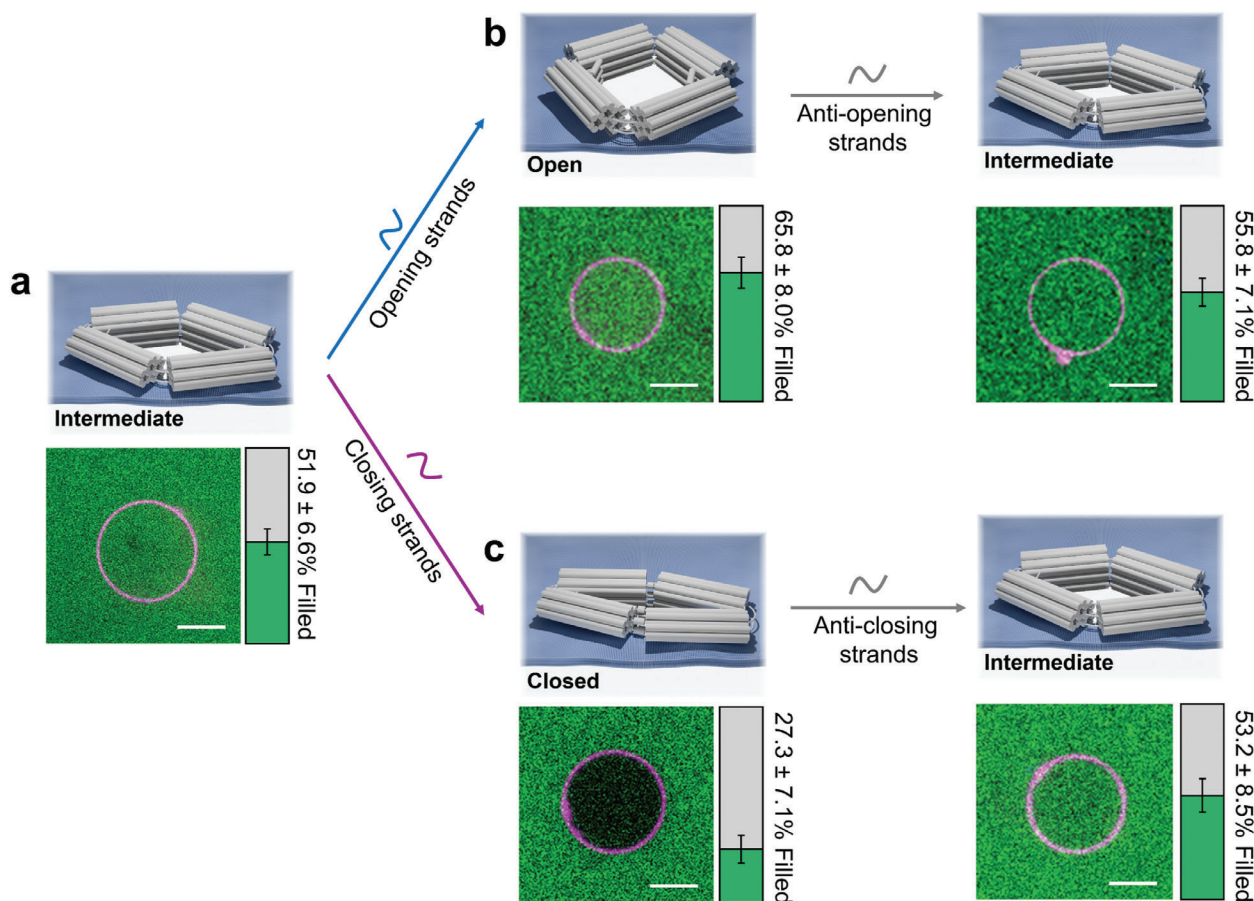
Figure 6. Reversible conformational changes of MPs embedded in GUVs and their permeability. Schematic representation (top) and confocal image (bottom) of a) the intermediate state with 70 kDa FITC-dextran, b) i → o → i switching, when adding opening and subsequently anti-opening strands, followed by 70 kDa FITC-dextran addition, and c) i → c → i switching when adding the closing and subsequently anti-closing strands followed by 70 kDa FITC-dextran addition. The distribution and percentage of filled GUVs in the dye influx experiments is shown in the respective colour bars. Green: filled, and grey: unfilled. Error bars: S.D.; N > 150 for 3 different experiments. Scale bars: 5 µm. N.B.: in all cases dextrans were added after addition of the respective trigger strands.

switching at individual nanopore levels by accurately monitoring the states of the MPs via 3D-DNA-PAINT, which enables the distinction between open, intermediate, and closed conformations. We additionally successfully demonstrate reversible nanomechanical cycling in GUVs using confocal imaging of dye influx assays.

The various stable configurations (open, intermediate, closed) within the lipid bilayer result in vastly different enclosed lumen sizes, allowing for the passage/transport of large molecules in the open state of the nanopores, yet also enabling the effective exclusion of small molecules from transmembrane passage if the very same nanopores are switched to their closed state. By employing FITC-dextrans of various sizes ranging from 6 to 22 nm in diameter, we clearly observe size-selective transport of molecules, with higher percentages of GUV filling for the most open MP configuration, and conversely blocked transport for smaller pore diameters (apart from the smallest measured 10 kDa dextrans). We note that the MP design is highly versatile, enabling the generation of nanopores with a range of stable lumen dimensions by simply changing the length of the triggers. We thus expect that this approach can be readily extended to molecular sieving applications that require even finer control of translocation sizes.

Our results demonstrate the potential of structurally adaptable DNA origami nanopores for applications in molecular delivery, sorting, and biosensing. We anticipate that our findings will pave the way toward more advanced dynamic nanodevices with potential uses in the field of controlled drug delivery and molecular diagnostics, as well as biomimetics and synthetic cell research, where controlled transport of biological macromolecules through large, stable channels is crucial. We thus highlight the wide applicability of these nanopores for both fundamental and applied biophysics research.

4. Experimental Section

DNA Origami Folding and Purification: The DNA origami nanopore was assembled using 15 nM of the scaffold p8634, and 100 nM of each staple strand in a buffer containing 5 mM Tris, 1 mM EDTA (pH 8), and 20 mM MgCl$_2$. The mixture was subjected to a thermal annealing ramp with a starting temperature of 65 °C (incubation for 5 min) and subsequent cooling to 20 °C over a period of 20 h. All additional handle staples

**ADVANCED
SCIENCE NEWS**

www.advancedsciencenews.com

**ADVANCED
MATERIALS**

www.advmat.de

were included in the folding mixture (see Figures S1 and S2 and Table S1 (Supporting Information) for handle positions and sequences).

Purification of the folded DNA origami nanoactuators from excess staple strands was achieved using ultrafiltration with 0.5 mL Amicon centrifugal filter units with 100 kDa molecular weight cut-off (Merck Millipore). The filter units were pre-washed with buffer (1x TAE, 5 mM MgCl$_2$), then the folding solution was loaded into the filters and centrifuged at 5000 rcf for 6–8 min. This step was repeated at least five times with fresh buffer (1x TAE, 5 mM MgCl$_2$) added in every centrifugation round.

Switching of the nanoactuators in solution was carried out by incubating the folded DNA origami with a 10-fold molar excess of the respective trigger strands at 33 °C for 3 h.

Transmission Electron Microscopy (TEM) Imaging: After the DNA origami nanostructures were diluted to 10 nM concentration, 10 µL of DNA origami solution were incubated for 2 min on a carbon-coated copper grid (Plano GmbH, Formvar/carbon 300 mesh) that had been plasma-cleaned for 30 s. For nanopore-containing GUV samples, an additional 2 min incubation time was required. The solution was then removed with the help of filter paper and the grid was stained with 5 µL of 2% uranyl formate solution for 45 s. Images were obtained on a Jeol-JEM-1230 TEM operating at an acceleration voltage of 80 kV. RELION 3 (https://relion.readthedocs.io/) was used to do the 2D classification analysis.

Atomic Force Microscopy (AFM) Measurements of Nanopore-Containing GUV Samples: AFM imaging was performed with a NanoWizard 4 (JPK Instrument AG) in QI mode in 1 x TAE buffer with 10 mM MgCl$_2$ using SCANASYST-FLUID+ probe (Bruker, Si N-type; L: 70 µm, W: 10 µm, T: 2 µm; Spring constant: 0.7 N m^{-1}). 5 µL of the sample was deposited on the fresh cleaved mica for 15 min, rinsed with 200 µL 1 x TAE buffer with 10 mM MgCl$_2$ 2 times. Image acquisition: with 256×256-pixel resolution.

Agarose Gel Electrophoresis: The DNA origami samples were diluted to 10 nM concentration in 1 x TAE buffer containing 5 mM MgCl$_2$ and then mixed with loading dye containing Orange G and glycerol. Subsequently, the samples were loaded onto a 2% agarose gel that was pre-stained with 0.01% Sybr Safe. The gel was run on ice for 150 min at 75 V (running buffer: 1 x TAE with 11 mM MgCl$_2$). Gel imaging was then carried out on a Typhoon FLA-9000.

DNA-PAINT Experiments: Microscope Setup: 3D fluorescence imaging with TIRF illumination was performed on the setup as described previously[36] using Hamamatsu, ORCA-Fusion BT, or Andor, Zyla 4.2 Plus sCMOS cameras.

Buffers: The following buffers were used for sample preparation and imaging (see also reference):[35]

- Buffer A: 10 mM Tris pH 8, 100 mM NaCl, and 0.05% Tween-20
- Buffer B: 10 mM MgCl$_2$, 5 mM Tris-HCl pH 8, 1 mM EDTA and 0.05% Tween-20, pH 8
- Buffer B20: 20 mM MgCl$_2$, 5 mM Tris-HCl pH 8, 1 mM EDTA and 0.05% Tween-20, pH 8
- 100x Trolox was made by adding 100 mg Trolox to 430 µl of 100% methanol and 345 µl of 1 M NaOH in 3.2 ml water.
- Imager solution: Buffer B20, 1x Trolox, pH 8, supplemented with Cy3B-coupled DNA imager strands.
- 20 nm grid DNA origami folding buffer: 10 mM Tris, 1 mM EDTA, 12.5 mM MgCl$_2$, pH 8
- FoB5 Buffer: 5 mM Tris, 1 mM EDTA, 5 mM MgCl$_2$, 5 mM NaCl, pH 8.5

20 nm Grid DNA Origami Self-Assembly and Purification: The 20 nm DNA origami grid was designed in Picasso's design module.[35] We followed the design used in Reinhardt et al.[36] and extended the 3′ ends of staple strands at the grid nodes with the docking strand sequence 7xR3 (CTCTCTCTCTCTCTCTCTCTC). The DNA origami was folded in a one-pot reaction (total volume: 40 µL) with 10 nM scaffold strand, 100 nM folding staples, 250 nM biotinylated staples, and 1 µM staple strands with docking site extensions in the folding buffer. In a thermocycler, the folding mix was incubated at 80 °C for 5 min prior to being gradually cooled from 80 to 65 °C in steps of 1 °C per 30 s and from 65 to 20 °C in steps of 1 °C per

1 min. Finally, the mix was incubated at 20 °C for 5 min and then held at 4 °C.

To purify the 20 nm grids we performed ultrafiltration with Amicon Ultra centrifugal filters (50 kDa MWCO; Merck Millipore, cat: UF505096). The filter units were equilibrated with 500 µL of FoB5 buffer and centrifuged at 10000 g for 5 min. The folded DNA origami was diluted to 500 µL with FoB5 buffer, added to the filters, and centrifuged for 3.5 min at 10000 g. After 2 additional washing steps with FoB5 buffer, the purified DNA origami was recovered by centrifugation for 5 min at 5000 g.

DNA Origami Sample Preparation and Imaging: The samples for DNA-PAINT measurements were prepared in a six-channel ibidi slide. First, 80 µl of BSA-biotin (1 mg mL^{-1}, dissolved in buffer A) were incubated in each channel for 5 min, followed by washing of the channels with 450 µl buffer A. In the next step, 100 µL of neutravidin (0.5 mg mL^{-1} in buffer A) was added to the channels for 5 min and then, the sample was washed first with 150 µL of buffer A and then with 450 µL of buffer B. Subsequently, gold nanoparticles (90 nm, diluted 1:19 in buffer B) were incubated on the slide for 5 min, followed by washing with 450 µL buffer B and a 5 min incubation of 80 µL of the 20 nm DNA origami grid structure (≈200 pM) (serving for drift correction and alignment of RESI rounds). Then, the channels were again flushed with 450 µL of buffer B, and the DNA origami nanopores equipped with biotin and handles for the DNA-PAINT imager strands (≈500 pM) were incubated in the channels for 5 min, followed again by washing with 450 µL of buffer B.

RESI imaging was conducted in 2 rounds, targeting the nanopore corner with the R4 extension in the first round and the corner with the R6 docking strand in the second round. For the first imaging round, 180 µl of the imager solution supplemented with 300 to 500 pM R4 imager (GTGTGT-Cy3B) and 100 to 150 pM R3 imager (GAGAGAG-Cy3B) was added to the sample into the channel. After the R4-R3 imaging round was completed, the sample was washed with buffer B20 until no residual blinking from the previous imager solution was detected. Then, the next imager solution supplemented with 1 to 1.5 nM R6 imager and 125 to 150 pM R3 imager was introduced and the second RESI round was acquired. For each round, 30 000 frames were acquired with an exposure time of 100 ms. The laser power was 40 mW at the objective.

DNA-PAINT Analysis: Super-resolution reconstruction was performed using the Picasso software[35] (https://github.com/jungmannlab/picasso). Drift was sequentially corrected, first by using gold particles as fiducials and then single DNA-PAINT docking sites. Alignment of both RESI rounds was performed with a redundant cross-correlation, followed by fiducial alignment using 20 nm grids.

Distance Measurements: The aligned data of the first (R3 & R4) and the second (R3 & R6) rounds were opened in Picasso Render. Regions of interest containing single nanopores with signals from both the R4 and the R6 sites were manually selected in Picasso for further analysis. RESI analysis was performed by applying Density-Based Spatial Clustering of Applications with Noise (DBSCAN)[41] for each round separately, yielding groups of localizations, where each group originates from an individual binding site. Only regions where exactly one R4 and exactly one R6 group were detected were kept for further analysis. RESI localizations were calculated as previously described[36] as weighted means of the DNA-PAINT localization groups achieving an average precision of 0.76 nm. Finally, the Euclidian distance between the R4 and R6 sites, representing the opening distance of the pore, was calculated within each region of interest.

Fluorescence Experiments: cDICE Buffers and Solutions: The following buffers were used for cDICE preparation:

- Inner solution: 50 mM Tris-HCl pH 7.4, 5 mM MgCl$_2$, 15 µM 2 MDa dextran, 3 nM MechanoPores.
- Outer solution: ≈135 mM glucose in Milli-Q water, osmotically matched to the inner solution.
- Oil phase: silicone and mineral oil mixture (4:1 ratio) with lipids 0.2 mg mL^{-1}.

Preparation of Lipid-in-Oil Suspension: The lipid-in-oil suspension was prepared as described previously[38] and used immediately. 0.2 mg mL lipids (DOPC:DOPE-Atto390 = 99.9:0.1 in chloroform) were prepared in a round bottom flask and blow-dried with pure nitrogen. The lipids were then dissolved in anhydrous chloroform inside a glove box filled with pure nitrogen. A mixture of silicone and mineral oil in 4:1 ratio was freshly prepared and then added to the lipids dropwise while vortexing at 1400 rpm. The lipid-in-oil solution was then vortexed at 2800 rpm for 2 min and subsequently sonicated in an ice bath for a minimum of 15 min.

Imaging Wells and Passivation: The cover glass (24 × 60 mm) was first rinsed with ethanol and water and dried out by nitrogen flow. The bottom part of 1000 µL white pipette tips was cut and glued on the cover glass to serve as imaging wells. 200 µL BSA (5 mg mL^{-1}) was added to each imaging cell and incubated at room template for at least 30 min. BSA was gently removed from each well and the wells were rinsed with 200 µL outer solution before use.

cDICE Equipment and GUV Production: GUVs were prepared as in.[38] Briefly, the cDICE chamber was first set to rotate at 300 rpm. 500 µL outer solution and subsequently 6 mL of lipid-in-oil dispersion were added into the rotating chamber. The outer solution and oil phase were stacked as illustrated in Figure 4a. The tip of capillary tubing (100 µm, PEEK, 211633-3, BGB) was inserted into the oil dispersion within the rotating chamber. A syringe pump (Harvard Apparatus) set at 20 µL min^{-1} was used to continuously insert the inner aqueous solution into the oil phase. After all the solution was injected into the chamber, the rotation speed (voltage) was gently turned down. The chamber was slightly tilted, and the oil phase was then removed as much as possible (4 to 5 mL). The chamber was set aside, and tiled so that GUVs could sediment to the bottom of the chamber. After 30 min, GUVs were collected from the outer aqueous solution with a 200 uL pipette tip (cut off the shaped tip) and moved to an imaging well with BSA passivation for further fluorescence experiments.

Data Collection and Analysis: Spinning disk confocal laser microscopy (Nikon Eclipse Ti-2, 100× objective, Photometrics Kinetix sCMOS) with Nikon NIS software was used to acquire fluorescence images. FITC-dextran (10 kDa, 70 kDa, or 150 kDa) was gently mixed with GUVs to the final concentration of 2 µM. After 24 h incubation at room temperature, fluorescence was measured with 405, 488, and 640 nm excitation.

Reversible Conformational Changes and Influx: A batch of MP-I containing GUVs was divided into 5 samples with intermediate-state DNA nanoactuators as the baseline and each of the five batches was triggered to undergo a different set of conformational changes: 1) adding opening strand, 2) adding opening strand and anti-opening strand after a 2 h interval, 3) adding closing strand, 4) adding closing strand and anti-closing strand after a 2 h interval 5) adding buffer as blank. After that, FITC-dextran (70 kDa) was gently mixed with GUVs to the final concentration of 2 µM. After 24 h incubation at room temperature, the fluorescence was measured with 405, 488 , and 640 nm excitation.

Fluorescence images were analyzed and processed using ImageJ (v1.54d).

Fluorescence Recovery After Photobleaching (FRAP) Assay and Diffusion Model: To photobleach the FITC-dextran, a 488 nm laser (at 9.8 mW) was employed to scan over the region of interest. Immediately following the photobleaching event, frames were captured every 15 s to measure the recovery of the fluorescence signal.

Diffusion Model: The details of the diffusion model for nanopore were reported in Fragasso et al.[11] Briefly, the FRAP data were transferred to normalized intensity difference $I_{ndiff} = (I_{out} - I_{in}) / I_{out}$, and fitted with a diffusion model derived from Fick's law of diffusion:

$$\frac{c_{out} - c_{in}(t)}{c_{out}} = \left(1 - \frac{c_{in,\,start}}{c_{out}}\right) e^{-\left(\frac{D_{eff} A_p N_p}{V L_p}\right)t} \tag{1}$$

where $c_{in,start}/c_{out}$ and N_p were free parameters of the fit, all other parameters and constants are known or can be calculated. In particular, the area

of pore $A_p = 197.8$ nm^2 was obtained from TEM experiments (**Figure** S13, Supporting Information). V is the volume of the GUV, which can be calculated from the diameter obtained from confocal images. The channel length $L_p = 14$ nm is the height of the nanopore. The effective diffusion constant $D_{eff} = 0.1$ µm^2 s^{-1} of 70 kDa dextran was calculated using the formula from Dechadilok and Deen:[42]

$$\frac{D_{eff}}{D_{bulk}} = 1 + \frac{9}{8}\left(\frac{R_g}{R_p}\right) ln\left(\frac{R_g}{R_p}\right) - 1.56034\left(\frac{R_g}{R_p}\right) +$$

$$0.528155\left(\frac{R_g}{R_p}\right)^2 + 1.91521\left(\frac{R_g}{R_p}\right)^3 - 2.81903\left(\frac{R_g}{R_p}\right)^4 +$$

$$0.270788\left(\frac{R_g}{R_p}\right)^5 + 1.10115\left(\frac{R_g}{R_p}\right)^6 - 0.435933\left(\frac{R_g}{R_p}\right)^7 \tag{2}$$

where R_g is the gyration radius of the molecule (for 70 kDa dextran, $R_g = 7.5$ nm), R_p is the pore radius (here 10 nm), and D_{bulk} is the diffusion constant of the molecule in free solution (for 70 kDa dextran, $D_{bulk} = 45.87$ µm^2 s^{-1} as we were using low concentration).[43]

Immobilization Assay: The imaging wells were coated with 100 µL BSA/biotinylated BSA mixture (1:1, 1 mg mL^{-1}) at room temperature for at least 30 min. The BSA mixture was removed from each well, then 100 µL streptavidin (0.1 mg mL^{-1}) was added to the wells and incubated at room temperature for 5 min. After removing the streptavidin from the wells, they were rinsed with 200 µL of outer solution before use. The GUVs for immobilization were made from DOPC: DSPE-PEG(2000)-biotin: DOPE-Atto390 = 99.9:1:0.1 ratio (0.2 mg mL^{-1}). The GUVs with incorporated MPs were produced via cDICE and then moved to the above-described pre-treated imaging wells to carry out the fluorescence experiments.

Single Vesicle Tracking: Fluorescence images were acquired using spinning disk confocal laser microscopy (Nikon Eclipse Ti-2, 100× objective, Photometrics Kinetix sCMOS) Nikon NIS software. FITC-dextran (70 or 150 kDa) was gently mixed with the respective GUV sample to the final concentration of 2 µM. After 24 h incubation at room temperature, the fluorescence was measured with 405, 488, and 640 nm excitation. To photobleach the FITC-dextran, a 488 nm laser (at 9.8 mW) was employed to scan over the region of interest. To measure the recovery signal, frames were collected with 488 nm excitation every 15 s for 1 min, starting right after the photobleaching event. After that, frames were collected every 2 min. The trigger strands were diluted to 500 nM in the outer solution and gently added to the immobilized GUV samples to reach a final concentration of 30 nM. After adding the trigger strands and before each FRAP assay, the samples were measured with 640 nm excitation to confirm the presence of GUVs that were monitored in the previous measurement.

Statistical analysis: DNA-PAINT: Data pre-processing was carried out as described above (see sections "DNA-PAINT analysis" and "Distance measurements"). The data from the distance measurements was presented in histograms with a fitted normal distribution (Origin). The peak center and width of the normal distribution are given as µ ± σ (in nm). For Figures 3, Figure S8 and S9, Supporting Information more than 700 picked nanopores were analyzed from each dataset, while for Figure S10 (Supporting Information), the sample size was more than 400 nanopores for each switching round.

Fluorescence Experiments: Data processing was carried out as described in the Method section "Data collection and analysis" and "Reversible conformational changes and influx". The data from fluorescence intensity measurements was normalized by normalized intensity difference: $I_{ndiff} = (I_{out} - I_{in}) / I_{out}$ and presented in histograms with a fitted normal distribution (Origin). The peak center and width of the normal distribution are given as µ ± σ (in nm). For Figure S12 (Supporting Information), 446 GUVs were analyzed. For

**ADVANCED
SCIENCE NEWS**

www.advancedsciencenews.com

**ADVANCED
MATERIALS**

www.advmat.de

Figure 5 and Figure 6, more than 150 GUVs were analyzed for each dataset.

TEM: Data processing was carried out as described in the Method section "Transmission electron microscopy (TEM) imaging". For Figure 2, more than 100 picked nanopores for each state were analyzed to obtain their class average, inner area, and opening angles.

Supporting Information

Supporting Information is available from the Wiley Online Library or from the author.

Acknowledgements

Conflict of Interest

The authors declare no conflict of interest.

Data Availability Statement

The data that support the findings of this study are available in the supplementary material of this article.

Keywords

[1] S. Howorka, *Nat. Nanotechnol.* **2017**, *12*, 619.
[2] A. Dorey, S. Howorka, *Nat. Chem.* **2024**, *16*, 314.
[3] I. C. Nova, J. Ritmejeris, H. Brinkerhoff, T. J. R. Koenig, J. H. Gundlach, C. Dekker, *Nat. Biotechnol.* **2023**, *42*, 710.
[4] Y.-L. Ying, Z.-L. Hu, S. Zhang, Y. Qing, A. Fragasso, G. Maglia, A. Meller, H. Bayley, C. Dekker, Y.-T. Long, *Nat. Nanotechnol.* **2022**, *17*, 1136.
[5] P. D. E. Fisher, Q. Shen, B. Akpinar, L. K. Davis, K. K. H. Chung, D. Baddeley, A. Saric, T. J. Melia, B. W. Hoogenboom, C. Lin, C. P. Lusk, *ACS Nano* **2018**, *12*, 1508.
[6] C. Dekker, *Nat. Nanotechnol.* **2007**, *2*, 209.
[7] K. Shimizu, B. Mijiddorj, M. Usami, I. Mizoguchi, S. Yoshida, S. Akayama, Y. Hamada, A. Ohyama, K. Usui, I. Kawamura, R. Kawano, *Nat. Nanotechnol.* **2022**, *17*, 67.
[8] Y. Xing, A. Rottensteiner, J. Ciccone, S. Howorka, *Angew. Chem., Int. Ed.* **2023**, *62*, 202303103.
[9] Y. Xing, A. Dorey, L. Jayasinghe, S. Howorka, *Nat. Nanotechnol.* **2022**, *17*, 708.
[10] Q. Shen, Q. Xiong, K. Zhou, Q. Feng, L. Liu, T. Tian, C. Wu, Y. Xiong, T. J. Melia, C. P. Lusk, C. Lin, *J. Am. Chem. Soc.* **2022**, *145*, 1292.
[11] A. Fragasso, N. De Franceschi, P. Stömmer, E. O. van der Sluis, H. Dietz, C. Dekker, *ACS Nano* **2021**, *15*, 12768.
[12] S. Dey, A. Dorey, L. Abraham, Y. Xing, I. Zhang, F. Zhang, S. Howorka, H. Yan, *Nat. Comm.* **2022**, *13*, 2271.
[13] P. W. K. Rothemund, *Nature* **2006**, *440*, 297.
[14] S. M. Douglas, H. Dietz, T. Liedl, B. Högberg, F. Graf, W. M. Shih, *Nature* **2009**, *459*, 414.
[15] B. Shen, P. Piskunen, S. Nummelin, Q. Liu, M. A. Kostiainen, V. Linko, *ACS Appl. Mater. Interfaces* **2020**, *3*, 5606.
[16] C. Lanphere, J. Ciccone, A. Dorey, N. Hagleitner-Ertuğrul, D. Knyazev, S. Haider, S. Howorka, *J. Am. Chem. Soc.* **2022**, *144*, 4333.
[17] M. Langecker, V. Arnaut, T. G. Martin, J. List, S. Renner, M. Mayer, H. Dietz, F. C. Simmel, *Science* **2012**, *338*, 932.
[18] S. Iwabuchi, I. Kawamata, S. Murata, S. M. Nomura, *Chem. Commun.* **2021**, *57*, 2990.
[19] S. Hernández-Ainsa, U. F. Keyser, *Nanoscale* **2014**, *6*, 14121.
[20] K. Göpfrich, A. Ohmann, U. F. Keyser, *Methods Mol. Biol.* **2021**, *2186*, 33.
[21] K. Göpfrich, C.-Y. Li, M. Ricci, S. P. Bhamidimarri, J. Yoo, B. Gyenes, A. Ohmann, M. Winterhalter, A. Aksimentiev, U. F. Keyser, *ACS Nano* **2016**, *10*, 8207.
[22] R. P. Thomsen, M. G. Malle, A. H. Okholm, S. Krishnan, S. S.-R. Bohr, R. S. Sørensen, O. Ries, S. Vogel, F. C. Simmel, N. S. Hatzakis, J. Kjems, *Nat. Comm.* **2019**, *10*, 5655.
[23] T. Diederichs, G. Pugh, A. Dorey, Y. Xing, J. R. Burns, Q. Hung Nguyen, M. Tornow, R. Tampé, S. Howorka, *Nat. Comm.* **2019**, *10*, 5018.
[24] J. R. Burns, A. Seifert, N. Fertig, S. Howorka, *Nat. Nanotechnol.* **2016**, *11*, 152.
[25] Y. Xing, A. Dorey, S. Howorka, *Adv. Mater.* **2023**, *35*, 2300589.
[26] J. J. Funke, H. Dietz, *Nat. Nanotechnol.* **2015**, *11*, 47.
[27] L. Zhou, A. E. Marras, H.-J. Su, C. E. Castro, *ACS Nano* **2013**, *8*, 27.
[28] A. Kucinic, C. M. Huang, J. Wang, H. J. Su, C. E. Castro, *Nanoscale* **2023**, *15*, 562.
[29] A. E. Marras, L. Zhou, H.-J. Su, C. E. Castro, *Proc. Natl. Acad. Sci.* **2015**, *112*, 713.
[30] M. Centola, E. Poppleton, S. Ray, M. Centola, R. Welty, J. Valero, N. G. Walter, P. Šulc, M. Famulok, *Nat. Nanotechnol.* **2023**, *19*, 226.
[31] Y. Ke, T. Meyer, W. M. Shih, G. Bellot, *Nat. Comm.* **2016**, *7*, 10935.
[32] K. Watanabe, I. Kawamata, S. Murata, Y. Suzuki, *JACS Au* **2023**, *3*, 1435.
[33] S. M. Douglas, A. H. Marblestone, S. Teerapittayanon, A. Vazquez, G. M. Church, W. M. Shih, *Nucleic Acids Res.* **2009**, *37*, 5001.
[34] J. K. Daljit Singh, M. T. Luu, J. F. Berengut, A. Abbas, M. A. B. Baker, S. F. J. Wickham, *Membranes* **2021**, *11*, 950.
[35] J. Schnitzbauer, M. T. Strauss, T. Schlichthaerle, F. Schueder, R. Jungmann, *Nat. Protoc.* **2017**, *12*, 1198.
[36] S. C. M. Reinhardt, L. A. Masullo, I. Baudrexel, P. R. Steen, R. Kowalewski, A. S. Eklund, S. Strauss, E. M. Unterauer, T. Schlichthaerle, M. T. Strauss, C. Klein, R. Jungmann, *Nature* **2023**, *617*, 711.

**ADVANCED
SCIENCE NEWS**

www.advancedsciencenews.com

**ADVANCED
MATERIALS**

www.advmat.de

[37] R. Jungmann, M. S. Avendaño, J. B. Woehrstein, M. Dai, W. M. Shih, P. Yin, *Nat. Methods* **2014**, *11*, 106.

[38] L. Van de Cauter, F. Fanalista, L. van Buren, N. De Franceschi, E. Godino, S. Bouw, C. Danelon, C. Dekker, G. H. Koenderink, K. A. Ganzinger, *ACS Synth. Biol.* **2021**, *10*, 1690.

[39] E. Baykal-Caglar, E. Hassan-Zadeh, B. Saremi, J. Huang, *Biochim. Biophys. Acta, Biomembr.* **2012**, *1818*, 2598.

[40] R. Hanselmann, W. Burchard, R. Lemmes, D. Schwengers, *Macromol. Chem. Phys.* **1995**, *196*, 2259.

[41] M. Ester, H.-P. Kriegel, X. Xu, *In Kdd* **1996**, *96*, 226.

[42] P. Dechadilok, W. M. Deen, *Ind. Eng. Chem. Res.* **2006**, *45*, 6953.

[43] M. B. Albro, V. Rajan, R. Li, C. T. Hung, G. A. Ateshian, *Cell. Mol. Bioeng.* **2009**, *2*, 295.

2405104 (14 of 14)